AGU PUBLICATIONS

JGR

Journal of Geophysical Research: Solid Earth

RESEARCH ARTICLE
10.1002/2014JB011260

This article is a companion to *Yarushina and Podladchikov* [2015] doi:10.1002/2014JB011258.

Key Points:
- The propagation of solitary waves in porous viscoplastic media is studied
- Viscoplastic rheological asymmetry leads to the channeling of fluid flow
- Plasticity affects wavelength, fluid overpressure, and amplitude of the porosity wave

Correspondence to:
V. M. Yarushina,
viktoriya.yarushina@ife.no

Citation:
Yarushina, V. M., Y. Y. Podladchikov, and J. A. D. Connolly (2015), (De)compaction of porous viscoelastoplastic media: Solitary porosity waves, *J. Geophys. Res. Solid Earth*, *120*, 4843–4862, doi:10.1002/2014JB011260.

Received 12 MAY 2014
Accepted 19 JUN 2015
Accepted article online 23 JUN 2015
Published online 14 JUL 2015

(De)compaction of porous viscoelastoplastic media: Solitary porosity waves

Viktoriya M. Yarushina[1], Yuri Y. Podladchikov[2], and James A. D. Connolly[3]

[1]Institute for Energy Technology, Kjeller, Norway, [2]Institut des Sciences de la Terre, University of Lausanne, Lausanne, Switzerland, [3]Earth Sciences Department, ETH Zurich, Zurich, Switzerland

Abstract Buoyancy-driven flow in deformable porous media is important for understanding sedimentary compaction as well as magmatic and metamorphic differentiation processes. Here mathematical analysis of the viscoplastic compaction equations is used to develop an understanding of the porosity wave instability and its sensitivity to the choice of rheological model. The conditions of propagation, size, speed, and shape of the porosity waves depend strongly on the properties of the solid rock frame. Whereas most of the previous studies on porosity waves were focused on viscous or viscoelastic mode, here we consider the ability of a solid matrix to undergo simultaneous plastic (rate-independent) and viscous (rate-dependent) deformation in parallel. Plastic yielding is identified as a cause of compaction-decompaction asymmetry in porous media—this is known to lead to a strong focusing of porous flow. Speed and amplitude of a porosity wave are given as functions of material parameters and a volume of a source region. Formulation is applicable to fluid flow in sedimentary rocks where viscous deformation is due to pressure solution as well as in deep crustal or upper mantle rocks deforming in a semibrittle regime.

1. Introduction

Two-phase models of fluid flow in deformable porous media are widely used to explain the various processes that occur in the Earth's interior and subsurface. The traditional fields include tectonic motion, crustal evolution, Earth's formation, petroleum and deepwater migration, and many other problems. However, attempts to model geological processes based on models of porous flow sometimes face issues in that the rate of fluid ascent predicted by the model is too low to adequately explain the observations. The oceanic crust covering two thirds of the Earth's surface is formed by extracting a small-degree partial melt at rates several orders of magnitude faster than predicted by the well-established models for pervasive porous flow [*McKenzie*, 2000; *Slater et al.*, 2001]. A similar problem is reported for the remaining one third of the Earth's surface—the continental crust that is partly formed by granitoid batholiths. Segregation of granitic magmas is estimated to have taken at the very least 2 orders of magnitude longer than the likely maximum duration of the melting event due to a high melt viscosity [*Wickham*, 1987]. Similarly, fast rates of primary petroleum migration necessitate reconsideration of the mechanisms by which hydrocarbons move from source beds to carrier beds and reservoirs [*Appold and Nunn*, 2002]. Numerous gas chimneys and pipes in marine sediments also indicate very rapid upward fluid migration on a time scale of hours to weeks [*Loseth et al.*, 2011; *Plaza-Faverola et al.*, 2011].

Interestingly, the "secondary" migration of the hydrocarbons, i.e., their flow in the carrier beds and reservoirs on time scales of exploration and production, is relatively well quantified by current reservoir simulators [*Sayers and Schutjens*, 2007; *Wurbs*, 1993]. These simulators are based on well-developed groundwater flow models and soil mechanics consolidation theory pioneered by *von Terzaghi* [1923]. These classical models treat compaction as rate-independent poroelastic or elastoplastic. This treatment is often referred to as "mechanical compaction" to discriminate it from "chemical compaction," which is rate dependent and mathematically equivalent to the compaction of Newtonian viscous materials. Chemical compaction is a thermally activated process and becomes important at a few kilometers of depth. In some cases, however, these two processes can act in parallel. The literature [*Appold and Nunn*, 2002] has discussed the Gulf of Mexico basin as an example where the hydrocarbons travel rather fast from the source sediments into the traps in the reservoirs. In this example, mechanical compaction models are sufficient for the shallower traps, but the problem of primary migration through the high-temperature deep source rocks may be related to viscous-like chemical compaction.

Viscous compaction of fluid-filled porous media can trigger the propagation of solitary porosity waves, which travel with high speed versus the background Darcian flux. Such waves were previously observed in experiments where low-viscosity buoyant fluid was injected into the highly viscous matrix [*Olson and Christensen*, 1986; *Scott et al.*, 1986] and most recently in experiments where a buoyant viscous fluid was injected into a mixture of deformable hydrogel beads submerged in viscous fluid [*Kumagai and Kurita*, 2015].

Most of the previous theoretical research on this phenomenon has focused on its implications for magma transport [*Connolly and Podladchikov*, 2007], but increasing recognition that the compaction of viscous porous media can occur in sedimentary basins has suggested the possibility that porosity waves could similarly be important for hydrocarbon and CO_2 transport [*Appold and Nunn*, 2002; *Connolly and Podladchikov*, 2000; *Raess et al.*, 2014]. Unlike pervasive background flow that exploits existing porosity, fluid-carrying porosity waves move through a void space that propagates or grows dynamically. While it is accepted that porosity waves can accelerate at least the initial stages of pore fluid segregation [*Richter and Mckenzie*, 1984; *Scott and Stevenson*, 1984], their role in efficient transport is much less clear. It is believed that even though the porosity waves do propagate faster than the background flow, their speed is still not high enough to explain the rapid melt ascent [*McKenzie*, 2000; *Slater et al.*, 2001].

However, this argument holds only for simple viscous models that treat decompaction in the same way as compaction. There is growing evidence that rocks respond differently to compaction and decompaction [*Nguyen et al.*, 2011]. Assuming the existence of such a rheology, *Connolly and Podladchikov* [2007] have shown that rheological asymmetry leads to a mechanical flow channeling instability propagating upward with high velocity. These authors used the simplest bilinear functional form to approximate effective viscosity. In this study, we utilize viscoplastic compaction rheological relationships derived from methods of effective media theory and analyze their impact on the existence of the porosity wave-like solutions of the compaction equations.

2. One-Dimensional Compaction: Mathematical Formulation

Equations governing the behavior of fluid-filled porous materials have been developed in a number of studies [*Bercovici et al.*, 2001; *Biot*, 1941; *Mckenzie*, 1984; *Scott and Stevenson*, 1984]. Earlier [*Yarushina and Podladchikov*, 2015], we proposed a new model for porous viscoelastoplastic materials filled with a fluid. It is based on the standard balance equations for mass, momentum, entropy, and energy written for fluid and solid phases. Admissible expressions for fluxes and sources are chosen in such a way that the first and second laws of thermodynamics be enforced. Classical nonequilibrium thermodynamics approaches were modified to account for dissipative and path-dependent processes such as irreversible rate-independent (plastic) deformation and difference in rock behavior during compaction and decompaction (decompaction weakening). The mechanical closure relationships were obtained from interpretation of the microstructure considering the evolution of noninteracting pores of cylindrical and spherical shape. It was shown that elastic, viscous, and elastoplastic end-members of the proposed viscoelastoplastic theory are consistent with experimentally verified models.

In this paper, we apply the developed formalism to study the effect of complex rheologies on developing porosity waves in fluid-filled porous media. We assume thermal and phase equilibria and consider only equilibrium mass exchange between the phases. This is true only when the rate at which mass is transferred from one phase to another is zero. The effect of simultaneous melting on compaction has been studied in *Schmeling* [2000] and *Sramek et al.* [2007]. Porosity waves in a viscous matrix with damage from magma fracturing during melt migration are also considered in *Cai and Bercovici* [2013]. Fluid flow in reactive systems is given in the literature [e.g., *Aharonov et al.*, 1997; *Connolly*, 1997; *Tantserev et al.*, 2009; *Tian and Ague*, 2014]. The effect of shear stresses on compaction of porous media is neglected. It is known that the presence of fluids does not affect shear properties of porous materials [*Gassmann*, 1951]. *Scott and Stevenson* [1986] and *Scott and Stevenson* [1984] using linear stability analysis and numerical modeling showed that finite shear viscosities influence porosity wave properties but do not affect the qualitative behavior and scaling predicted from the compaction equations.

Most of these publications describe isothermal compaction of porous media with incompressible constituents by fluid and solid mass conservation equations:

$$\frac{\partial(1-\varphi)}{\partial t}+\nabla_j\left((1-\varphi)v_j^s\right)=0 \tag{1}$$

Table 1. Common Symbols and Their Definitions

Symbol	Meaning	Units
$h(\varphi)$	Hydraulic potential, equation (22)	
k, k_0	Permeability, equation (14); reference value at φ_0	m^2
L^*	Compaction length scale, equation (34)	m
m, $\widetilde{m}$	Pore geometry indicator; $m=1$, $\widetilde{m}=1$ for cylindrical pores and $m=2$, $\widetilde{m}=4/3$ for spherical pores	
n	Permeability porosity exponent, equation (14)	
p^s, p^f	Solid and fluid pressures	Pa
$\overline{p}$, p_e	Total pressure; effective pressure	Pa
p^*	Characteristic pressure scale, equation (35)	Pa
q_s, q_f	Fluxes of fluid and solid matter	$m\,s^{-1}$
v_j^s, v_j^f	Components of the velocity vector in solid and fluid	$m\,s^{-1}$
V_{exc}	Amount of fluid filled porosity in excess to a background level	m
ω	Dimensionless sedimentation parameter (phase velocity of porosity wave)	
Y	Yield stress for frictionless materials and cohesion for frictional materials	Pa
$\hat{z}$, z	Upward directed unit vector; vertical depth coordinate	m
φ	Internal angle of friction	
φ, φ_0	Porosity; background value of porosity	
η_s, η_f, η_φ	Shear viscosity of solid mineral grains; fluid shear viscosity; effective viscosity of porous aggregate	Pa s
ρ^s, ρ^f, $\Delta\rho$	Solid density; fluid density; $\rho^s-\rho^f$	$kg\,m^{-3}$
ξ	Direction of loading, $\xi=1$ for compaction, $\xi=-1$ for decompaction	
ψ	Angle of dilation	

$$\frac{\partial\varphi}{\partial t}+\nabla_j\left(\varphi\ v_j^f\right)=0 \tag{2}$$

and total force balance equation in the presence of the gravity field:

$$\nabla_j\overline{\sigma}_{ij}-g\overline{\rho}\hat{z}^i=0.$$

In the absence of shear stresses ($\overline{\sigma}_{ij}=-\overline{p}\delta_{ij}$, $\sigma_{ij}^f=-p^f\delta_{ij}$, and $\sigma_{ij}^s=-p^s\delta_{ij}$), the latter reduces to

$$\nabla_i\overline{p}+g\overline{\rho}\hat{z}^i=0. \tag{3}$$

These must be accompanied by Darcy's law

$$\varphi\left(v_i^f-v_i^s\right)=-\frac{k}{\eta_f}\left(\nabla_i p^f+g\rho^f\hat{z}^i\right) \tag{4}$$

and the porosity equation of the form

$$p_e=-\eta_\varphi\,\dot{\varphi}, \tag{5}$$

where φ is the porosity, η_φ is the effective viscosity, k is the matrix permeability, g is the gravity, $\hat{z}^i$ are the components of an upward directed unit vector, and ∇_j are the components of the del operator. The superscript and subscript f and s distinguish the fluid and solid velocities, v_j; densities, ρ; stresses, σ_{ij}; and pressures, p (see Table 1 for notations). The bar represents the total values of corresponding quantities so that $\bar{a}=a^f\varphi+a^s(1-\varphi)$. The upper dot marks the material time derivatives ($d/dt=\partial/\partial t+v_j\nabla_j$). Effective pressure is defined as

$$p_e=\overline{p}-p^f=\left(p^s-p^f\right)(1-\varphi). \tag{6}$$

Although the solid and fluid components are incompressible, the matrix is compressible because fluid may be expelled from the pore volume. Effective bulk viscosity η_φ reflects properties of porous rock and depends on the viscous and failure parameters of the mineral grains composing the rock as well as on the pore structure. In our previous paper [*Yarushina and Podladchikov*, 2015], we derived a functional form of the effective viscosity based on simplifying assumptions about the geometry of the pore space. Table 2 gives an overview of the results for various types of rock rheologies. At low to moderate stresses, the rocks behave in a linear viscous manner, which can be due to pressure solution or diffusion creep. At higher stress levels, rocks start to fail and exhibit permanent plastic deformation (yielding). Hence, viscous and plastic deformation mechanisms act in parallel leading to viscoplastic pore collapse in porous rocks. We consider two end-members of plastic deformation mechanisms: (1) pressure-sensitive yield, which we term further as dilatant brittle failure, and (2) pressure-insensitive yield. Dilatant brittle failure is due to

Table 2. Effective Bulk Viscosity: Summary From *Yarushina and Podladchikov* [2015]

Viscous: $\eta_\phi = \widetilde{m}\eta_s/\phi$

Viscoplastic: Pressure-insensitive yielding	
$\eta_\phi = \frac{\eta_s}{\phi(1-\phi)R}\cdot\left\lvert\frac{p_e}{Y}\right\rvert$	$1-\varphi \le \left\lvert\frac{p_e}{\widetilde{m}Y}\right\rvert \le \ln\frac{1}{\varphi}$
where $\left\lvert\frac{p_e}{\widetilde{m}Y}\right\rvert = 1+\ln R - R\varphi$	
$\eta_\phi = \frac{\eta_s}{\phi}\cdot\lvert\frac{p_e}{Y}\rvert\cdot\exp\left(1-\left\lvert\frac{p_e}{\widetilde{m}Y}\right\rvert\right)$	$\varphi << 1,\ \lvert p_e\rvert \ge \widetilde{m}Y$
Viscoplastic: Dilatant brittle failure	
$\eta_\phi = \frac{2\kappa\eta_s}{\phi}\frac{p_e}{Y^*}\left(1-\phi\widetilde{P}^\chi + \frac{\chi}{\gamma}\left(\widetilde{P}^\gamma - 1\right)\right)^{-1}$	$\frac{\widetilde{m}}{2\kappa}(1-\phi) \le \frac{p_e}{Y^*} \le \frac{1}{\kappa-1}\left(1-\phi^{\frac{\widetilde{m}(\kappa-1)}{2\kappa}}\right)$
where $\widetilde{P} = 2\kappa m\widetilde{m}\frac{1+(1-\kappa)p_e/Y^*}{\kappa+m\left(1+\varphi(\kappa-1)R^{2\kappa/\widetilde{m}}\right)}$	
$\frac{1}{\kappa-1} + \frac{\widetilde{m}\chi}{2\kappa}R^{1-\kappa} - \frac{\widetilde{m}\varphi}{2\kappa}R^{\chi(1-\kappa)} = \frac{p_e}{Y^*}$	
$\eta_\phi = \frac{2\kappa\eta_s}{\varphi}\frac{p_e}{Y^*}\left(1+\frac{\chi}{\gamma}\left(\widetilde{P}^\gamma - 1\right)\right)^{-1}$	$\varphi << 1,\ \frac{p_e}{Y^*} \ge \frac{\widetilde{m}}{2\kappa}$
where $\widetilde{P} = \frac{2\kappa}{\widetilde{m}\chi(1-\kappa)}\left(1+(1-\kappa)\frac{p_e}{Y^*}\right)$	
Plastic pore collapse	
Pressure-insensitive yielding: $p_e = \widetilde{m}Y\xi\ln\frac{1}{\varphi}$	Dilatant brittle failure: $p_e = \frac{Y^*}{\kappa-1}\left(1-\varphi^{(\kappa-1)\frac{\widetilde{m}}{2\kappa}}\right)$

homogeneous cataclastic flow around pores governed by the Mohr-Coulomb criterion on a pore scale, and pressure-insensitive yield is due to crystal plasticity or mode II shear failure concentrated in the vicinity of pores. This is described by von Mises microscopic criterion. The viscoplastic deformation occurs when the effective pressures lie within a certain range of effective pressures.

2.1. One-Dimensional Steady State Isothermal Compaction of Porous Media With Incompressible Constituents

One- and two-dimensional equations for fluid flow in porous media with a compactable matrix have been studied [*Barcilon and Richter*, 1986; *Barcilon and Lovera*, 1989; *Connolly and Podladchikov*, 1998, 2000, 2007, 2015; *Richter and Mckenzie*, 1984; *Scott and Stevenson*, 1986; *Simpson and Weinstein*, 2008; *Spiegelman*, 1993; *Sumita et al.*, 1996]. These studies found that the shape of a two-dimensional solution along the vertical axis of symmetry is similar to a solution obtained for one-dimensional setup at high velocities [*Barcilon and Lovera*, 1989; *Connolly and Podladchikov*, 2007]. Therefore, many important features of multidimensional compaction can be studied in the simplified one-dimensional setup.

Porosity waves represent a special type of fluid flow instability. Their size, velocity, shape, and conditions of propagation depend strongly on the properties of the solid rock frame. Any alteration in the rock rheology can lead to variations in the properties of a porosity wave. Purely viscous rocks can accommodate a single solitary porosity wave or a periodic wave train, both of which propagate preserving shape and size [*Scott et al.*, 1986]. In viscoelastic porous rocks, both a single solitary wave and periodic waves are possible, but they would attenuate losing their energy and amplitude [*Connolly and Podladchikov*, 2000]. In poroelastic rocks, obstructions to fluid flow would generate shock waves that do not detach from the source *Rice* [1992]. If the rock requires less effort to open new porosity than to close already existing pores, then the so-called decompaction weakening takes place—this is responsible for strong focusing of the fluid flow [*Connolly and Podladchikov*, 2007]. Porosity waves in nonlinear viscous rocks with power law rheology are similar to the purely viscous porosity waves. However, wavelengths that determine the spatial focusing of the wave are significantly influenced by the power law exponent [*Connolly and Podladchikov*, 2013]. Nonlinearity amplifies the effects of temperature and upward strengthening of the crust on the porosity wave geometry, compaction length, and time scales. Thus, the existence of porosity waves in the general case of complex rock rheologies is not guaranteed, and their properties need to be investigated. In this paper, we consider the effect of plastic yielding in solid matrix on porosity waves. Plasticity adds strong nonlinearity into constitutive equations resulting in a different behavior of the solid matrix in the regimes of precritical viscous flow and plastic yielding. It also leads to compaction/decompaction asymmetry.

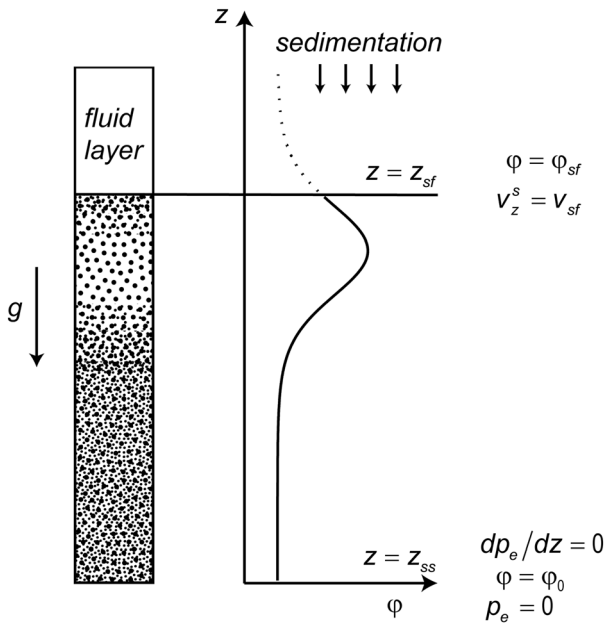

Figure 1. Problem setup for 1-D uniform sedimentation.

Numerical experiments show that over time a transient porosity wave evolves toward a steady state regime that can be studied as a stationary solution in compaction equations [*Connolly and Podladchikov*, 2000; *Vasilyev et al.*, 1998]. Therefore, we here investigate one-dimensional stationary solutions to compaction equations (1)–(5) of isothermal compaction of viscoplastic porous media with incompressible constituents. There are two different model problems that have similar mathematical descriptions and stationary porosity wave solutions—equilibrium compaction of sedimentary layer and a propagating upward fluid pocket.

2.2. Equilibrium Compaction (Uniform Sedimentation)

Equilibrium compaction or uniform sedimentation of a vertical column of fluid-saturated porous rock has been considered [*Connolly and Podladchikov*, 2000]. During sedimentation, low-density fluid segregates from deformable porous matrix. Over time, compaction in the upper part of the sedimentary column extending from the sediment-fluid interface ($z = z_{sf}$) to a depth, z_{ss}, evolves toward a steady state, while the porosity profile becomes independent of time and forms a part of a stationary porosity wave (Figure 1). Compaction is slow below $z = z_{ss}$ and therefore is still in the transient regime. We do not consider this here. One-dimensional stationary solutions to compaction equations (1)–(5) can be obtained by putting $\partial/\partial t = 0$ and replacing material time derivative in equation (5) with $d/dt = v_z^s d/dz$, where v_z^s is a vertical component of solid velocity.

2.2.1. Hydraulic Equation

In a steady state regime, conservation of mass for fluid and solid yields

$$\varphi v_z^f = -q_f \tag{7}$$

$$(1-\varphi)v_z^s = -q_s, \tag{8}$$

where q_f and q_s are the constant fluxes of fluid and solid, respectively. Boundary conditions at the solid-fluid interface (Figure 1) define solid flux, q_s, in terms of the sedimentation rate and surface porosity as

$$q_s = -(1-\varphi_{sf})v_{sf}. \tag{9}$$

Using equations (3) and (6), the Darcy's law can be rewritten in the form

$$\varphi\left(v_z^f - v_z^s\right) = \frac{k}{\eta_f}\left(\frac{dp_e}{dz} + (1-\varphi)g\Delta\rho\right), \tag{10}$$

where $\Delta\rho = \rho_s - \rho_f$. Equations (7)–(10), together with $z = z_{ss}$ (Figure 1), constrain fluid flux, so that

$$q_f = \frac{\varphi_0}{1-\varphi_0}q_s - \frac{k_0}{\eta_f}(1-\varphi_0)g\Delta\rho. \tag{11}$$

Substitution of equations (7), (8), and (11) into equation (10) leads to the following form of hydraulic equation:

$$\frac{dp_e}{dz} = \frac{\varphi-\varphi_0}{(1-\varphi_0)(1-\varphi)}\frac{q_s\eta_f}{k} + \Delta\rho g\left(\frac{k_0}{k}(1-\varphi_0) - (1-\varphi)\right), \tag{12}$$

where k_0 is a background permeability value.

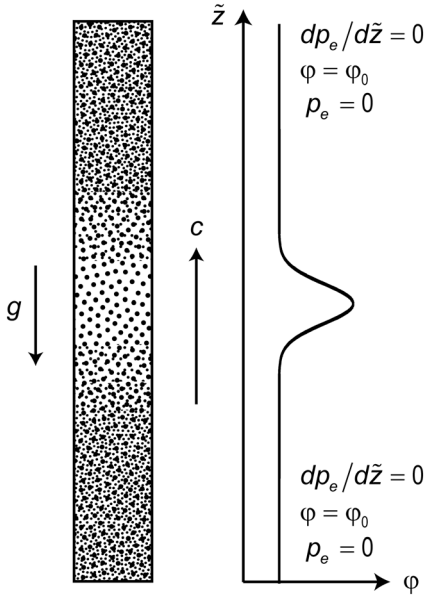

Figure 2. Problem setup for 1-D steady state propagation of porosity wave. A vertical column of porous rock with homogeneous porosity ϕ_0 is subsiding under its own weight, while steady porosity wave travels upward through the column with velocity c.

2.2.2. Rheology

The hydraulic equation alone cannot define the porous flow in a deformable solid matrix. The permeability law and the closure relationship governing the compaction of the matrix in the form of the porosity equation are needed. In a stationary regime, the porosity equation (5) takes the form:

$$\frac{d\varphi}{dz} = \frac{1-\varphi}{q_s}\frac{p_e}{\eta_\varphi}. \tag{13}$$

For permeability, we choose the expression:

$$k = k_0(\varphi/\varphi_0)^n, \tag{14}$$

where k_0 and φ_0 are the background values of the permeability and porosity, respectively; the exponent n is taken to be constant.

2.3. Propagating Upward Solitary Waves

A problem setup for a propagating upward fluid pocket during a uniform free subsidence of solid matrix is shown in Figure 2. A solitary porosity wave is initiated in response to a local alteration in porosity. A localized area of elevated porosity is formed above the disturbance and starts to propagate upward preserving its own shape. The background value of porosity φ_0 and zero effective pressure are restored below the wave (Figure 2). We introduce a coordinate frame that travels together with the porosity wave such that the porosity profile stays unchanged in this reference frame by substitution:

$$\tilde{z} = z - ct, \quad \frac{\partial}{\partial z} = \frac{d}{d\tilde{z}}, \quad \frac{\partial}{\partial t} = -c\frac{d}{d\tilde{z}}, \tag{15}$$

where c is the ascent velocity of a porosity wave. Assuming that the new frame of reference is barycentric (i.e., $\varphi v_z^f + (1-\varphi)v_z^s = 0$), the mass balance equations (1) and (2) lead to

$$v_z^f = c + \frac{q_s}{\varphi}, \quad v_z^s = -\frac{c\varphi + q_s}{1-\varphi}. \tag{16}$$

We also assume that the wave transition from the background porosity to disturbed state must be slow (i.e., $d\varphi/d\tilde{z} \to 0$ and $dp_e/d\tilde{z} \to 0$ at $z \to \pm\infty$). Thus, Darcy's law (equation (4)) and the porosity equation (5) becomes equation (17) via equation (16):

$$\frac{dp_e}{d\tilde{z}} = \frac{\varphi-\varphi_0}{(1-\varphi)}\frac{c\eta_f}{k} + \Delta\rho g\left(\frac{k_0}{k}\frac{(1-\varphi_0)^2}{1-\varphi} - (1-\varphi)\right) \tag{17}$$

$$\frac{d\varphi}{d\tilde{z}} = \frac{1-\varphi}{q_s + c}\frac{p_e}{\eta_\varphi}, \tag{18}$$

where

$$q_s = (1-\varphi_0)^2\Delta\rho g k_0/\eta_f - c\varphi_0.$$

Thus, it is clear that the two model problems of uniform sedimentation and propagating upward fluid pocket considered in sections 2.2 and 2.3 have similar mathematical formulations.

3. Steady State Compaction: Small-Porosity Approximation

With a given permeability law, equations (12) and (13) as well as equations (17) and (18) form a system of two ordinary differential equations for two unknowns p_e and φ. For simplicity, we adopt a small-porosity approximation, which implies that $1-\varphi \approx 1$ and $1-\varphi_0 \approx 1$. This is justified at initial stages of melt

segregation when porosities reach only a few tenths of a percent. We later verified this simplification by considering the full solution. At small porosities, equations (12) and (13) become

$$\frac{dp_e}{dz} = q_s \frac{\eta_f}{k}(\varphi - \varphi_0) + \Delta\rho g\left(\frac{k_0}{k} - 1\right) \tag{19}$$

$$\frac{d\varphi}{dz} = \frac{p_e}{q_s \eta_\varphi}. \tag{20}$$

Equations (17) and (18) also reduce to equations (19) and (20), where q_s is replaced with c in the hydraulic equation and with $c + q_s$ in the porosity equation. We further examine in detail equations (19) and (20) for uniform sedimentation. All of our results can be easily adapted to the case of propagating fluid pockets.

At the initial stages of melt segregation, the impact of porosity changes on effective viscosity is rather weak. In several studies focused on pure viscous materials [*Barcilon and Richter*, 1986; *Barcilon and Lovera*, 1989; *Mckenzie*, 1984], the bulk viscosity is assumed to be constant. This assumption simplifies the analysis of the governing equations while preserving the quantitative behavior of the solution. Following these previous works and for the sake of clarity we ignore the dependence of effective viscosity on porosity. For purely viscous materials, this means that the bulk viscosity is constant and depends on the viscosity of the solid grains, pore space geometry, and background porosity. In the viscoplastic case, the dependence on effective pressure is added. Under this assumption, compaction equations (19) and (20) become

$$\frac{dp_e}{dz} = -\frac{\partial h}{\partial \varphi}\Delta\rho g, \quad \frac{d\varphi}{dz} = f(p_e), \tag{21}$$

where h is a dimensionless hydraulic potential depending on porosity only:

$$-\frac{\partial h}{\partial \varphi} = \frac{k_0}{k} - 1 + \frac{q_s \eta_f}{k \Delta\rho g}(\varphi - \varphi_0). \tag{22}$$

The right-hand side of the porosity equation, $f(p_e)$, is a driving force for compaction given as

$$f(p_e) = \frac{p_e}{q_s \eta_\varphi(p_e)}. \tag{23}$$

In a purely viscous case, term $f(p_e)$ is a linear function of effective pressure.

3.1. Oscillating Ball Analogy

Before starting the rigorous analysis of equation (21) governing compaction-driven fluid flow we notice that another physical system has a similar mathematical description [see also *Connolly and Podladchikov*, 2015]. Imagine an initially stationary ball of mass m placed on a frictionless one-dimensional curved surface whose shape is described by function h representing the height of the surface as a function of the position x of the ball along this surface (Figure 3a). If the forces holding the ball at its initial position are removed, then the ball starts moving along surface h in response to gravity. Newton's second law and the kinematic relation describe its motion:

$$\frac{dv}{dt} = -\frac{\partial h}{\partial x}g, \quad \frac{dx}{dt} = v. \tag{24}$$

Here t is the time and v is the velocity along the surface. Equation (24) defines velocity and position as functions of the time. Using the following substitutions, compaction equation (21) can be converted into the oscillating ball equation (24) and vice versa:

compaction	oscillating ball
z	t
φ	x
$f(p_e)$	v
$\Delta\rho g$	g
h	h

We further utilized the similarity of both systems to study compaction using well-established mathematical tools for the oscillating ball system (see more on the oscillating ball analogy in the Appendix).

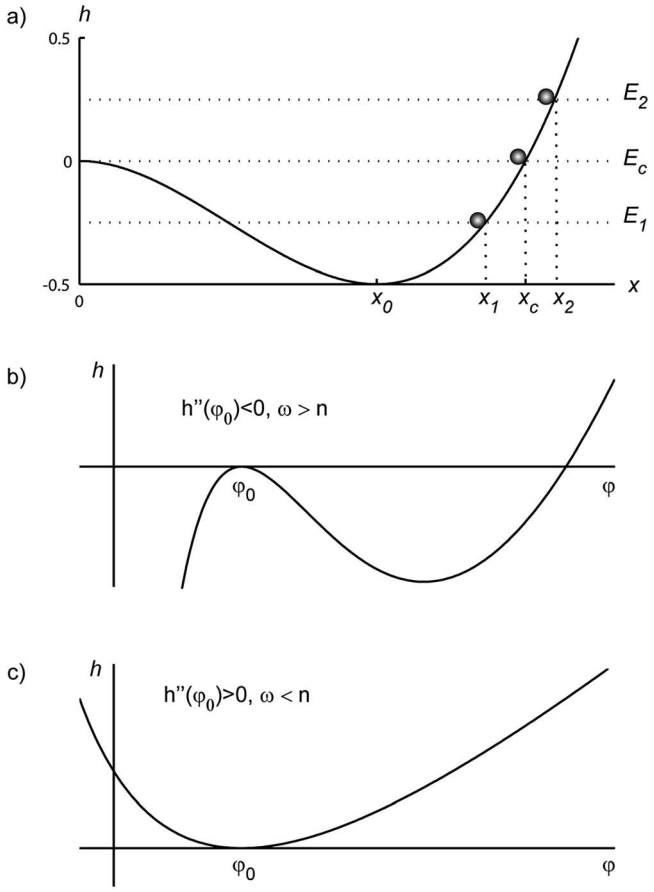

Figure 3. Oscillating ball analogy to compaction equations. (a) The ball of mass m is placed on a frictionless one-dimensional curved surface, which shape is described by function $h = x^2(x - 3/2x_0)$. There are three different possible initial positions of the ball: above the critical level E_c, below the critical level E_c, and exactly on E_c. (b) Hydraulic potential as a function of porosity corresponding to solitary wave solution. (c) Hydraulic potential as a function of porosity corresponding to oscillations of porosity around stable background level.

3.2. Viscous Matrix

By excluding depth from the compaction equations one can present pressure as a function of porosity (see Appendix for mathematical details).

$$f(p_e)\frac{dp_e}{d\phi} = -\frac{\partial h}{\partial \phi}\Delta\rho g.$$

Separation of variables in the last equation results in

$$f(p_e)dp_e = -\Delta\rho g\frac{\partial h}{\partial \phi}d\phi. \quad (25)$$

Subsequent integration leads to

$$E = \int f(p_e)dp_e + \Delta\rho g h. \quad (26)$$

The quantity E on the left-hand side of equation (26) is conserved along the trajectory. It has the dimension of *Pa*/*m* and represents the sum of the hydraulic gradient (the second term on the right) and the pressure gradient due to resistivity of the deformable solid matrix (the first term on the right). Porous flow in deformable rock is a result of competition between the hydraulic gradient and resistivity of the solid rock frame. As can be seen from equation (26), the hydraulic part stays unchanged for all rock types, while changes in rock rheology might significantly influence the first term.

In purely viscous porous rocks, the effective viscosity might be represented in the form [*Yarushina and Podladchikov*, 2015] (see also Table 2):

$$\eta_\varphi = \widetilde{m}\eta_s/\phi_0.$$

Here $\widetilde{m} = 1$ for cylindrical pores and $\widetilde{m} = 4/3$ for spherical ones. Substitution of this expression for effective viscosity into equation (25) together with equations (22) and (23) results in the following first integral for purely viscous compaction equations in a small-porosity approximation:

$$\frac{p_e^2}{2(p^*)^2} = \omega\widetilde{m}h(\varphi), \quad (27)$$

where

$$h(\varphi) = \frac{\omega + n(n-2)}{(n-1)(n-2)} - \frac{k_0}{k}\frac{\varphi}{\varphi_0}\left(\frac{\varphi}{\varphi_0}\frac{\omega}{n-2} - \frac{\omega-1}{n-1}\right) - \frac{\varphi}{\varphi_0} \quad (28)$$

is a hydraulic potential. Here we introduce compaction length (L^*) and the pressure difference due to buoyancy on this length scale (p^*) as follows:

$$L^* = \sqrt{\frac{k_0\eta_s}{\varphi_0\eta_f}}$$

$$p^* = \Delta\rho g L^*.$$

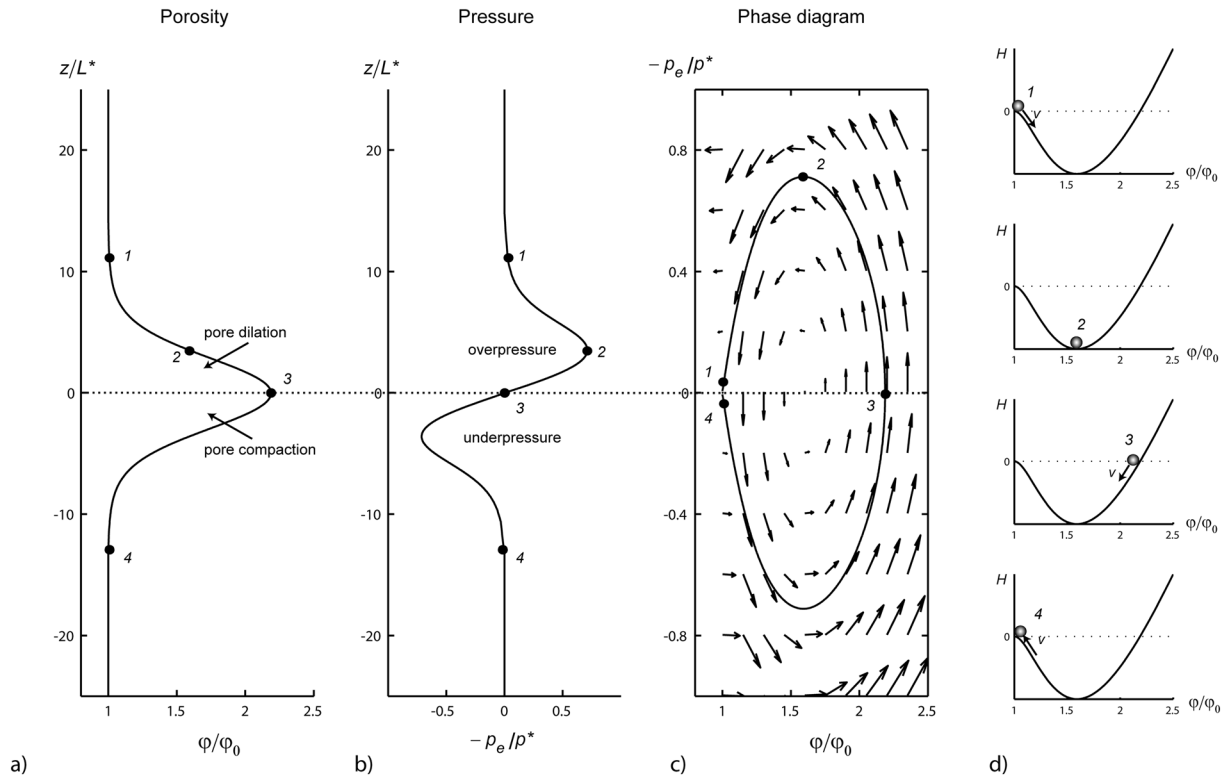

Figure 4. Purely viscous analytical stationary solution for porosity and effective pressure distribution within porosity wave (small-porosity approximation; $\omega = 5$, $n = 3$). (a) Porosity profile with depth in a barycentric frame, (b) effective pressure ($-p_e = p^f - \overline{p}$), (c) pressure-porosity phase diagram, and (d) oscillating ball analogy: positions of the ball corresponding to points 1–4 on the phase diagram.

Parameter

$$\omega = \frac{q_s \eta_f \varphi_0}{\Delta \rho g k_0}$$

gives the ratio of the solid flux, q_s, to the Darcy's flow rate, $\Delta\rho g k_0/(\eta_f \varphi_0)$. Large values of this parameter indicate rapid sedimentation or slow Darcy's flow rate (low hydraulic conductivity). Compaction equations can have different types of solutions depending on the functional form of the hydraulic potential (see Appendix for more details). By putting $\partial h/\partial\varphi = 0$ in equation (22), we find that h has at least one equilibrium point at $\varphi = \varphi_0$. It is the local maximum if $\omega > n$ ($h''(\varphi_0) < 0$) and the local minimum if $\omega < n$ ($h''(\varphi_0) > 0$). When $\omega < n$ and $n > 1$, the φ_0 is a point of stable equilibrium and any perturbations in the background porosity φ_0 lead to small oscillations around this value (Figure 3c). Compaction equations have a solitary wave solution only if φ_0 is a point of unstable equilibrium (Figure 3b), i.e.,

$$\omega > n > 1. \tag{29}$$

In other words, the porosity wave can only propagate when sedimentation is rapid in comparison to the Darcy's flow rate.

While phase trajectories on the (φ, p_e) plane give valuable information about the type of solution, numerical integration of equation (21) is required to obtain pressure and porosity profiles with depth. One of the solutions to Figure 4 shows a solitary wave solution to equation (21). Above the wavefront (point 1), homogeneous distribution of porosity is maintained under zero effective pressure. As the wave arrives, fluid overpressure starts to grow beneath the front (below point 1), causing the pore space to dilate until the resistance from the surrounding solid rock matrix limits the overpressure growth at point 2. After that, the fluid pressure reduces below the total pressure of the host rock and goes back to the initial background value at point 4. This causes compaction underneath the crest point back to the background porosity φ_0. The vectors on Figure 4c indicate gradients $\partial\varphi/\partial z$ and $\partial p_e/\partial z$—these are tangential to the trace of the stationary solution. For a solitary wave, the gradients of porosity and effective pressure do not converge as porosity and pressure decrease to background levels. The trace of a solitary solution

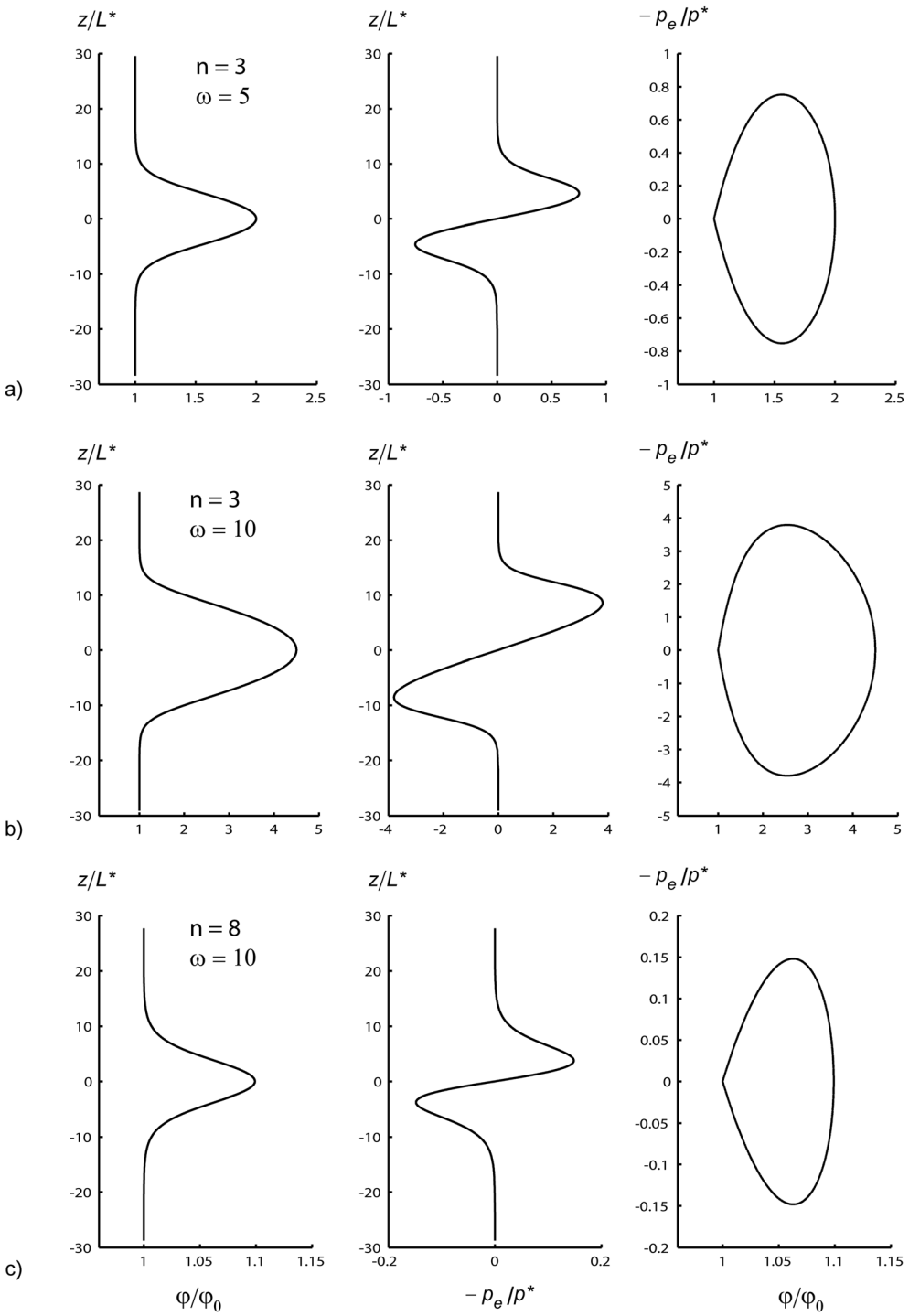

Figure 5. Purely viscous analytical stationary solution for porosity and effective pressure (small-porosity approximation) for different values of sedimentation parameter ω and permeability exponent n.

approaches point $p_e = 0$, $\varphi = \varphi_0$ asymptotically, i.e., at infinite distance from the wave center. (Please, notice positions of the oscillating ball corresponding to critical points on a solitary wave in Figure 4d.)

The amplitude and the wavelength of the solitary wave depend on material parameters (Figure 5). An increasing permeability exponent reduces the amplitude of the wave and the magnitude of wave anomaly (Figures 5a–5c). At the same time, an increasing ω leads to a stronger pressure anomaly and increases the

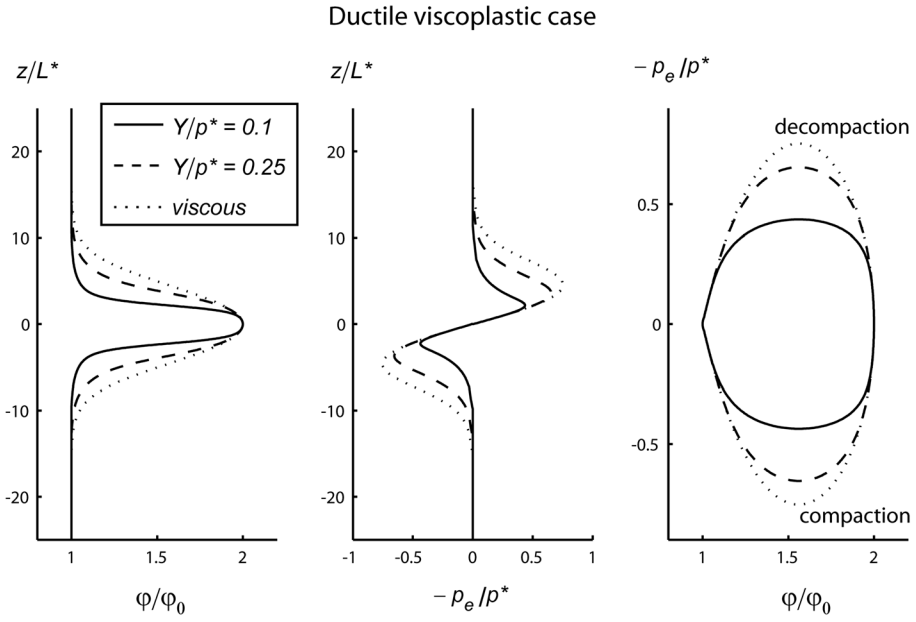

Figure 6. Analytical solution for porosity wave in a viscoplastic matrix with pressure-insensitive yielding ($\omega = 5$, $n = 3$): variations of porosity and effective pressure with depth and phase diagram. The solid and dashed lines correspond to the viscoplastic solution obtained for two different values of the yield stress. The dotted lines represent a purely viscous solution obtained for the same values of ω and n.

wavelength and the amplitude of the wave (Figures 5a and 5b). In other words, larger-amplitude porosity waves are generated in response to rapid burial of low-permeability sediments.

3.3. Pressure-Insensitive Viscoplastic Matrix

Effective viscosity in pressure-insensitive viscoplastic porous rocks takes the form [*Yarushina and Podladchikov*, 2015]:

$$\eta_\varphi = \begin{cases} \widetilde{m}\eta_s/\phi_0 & \text{if} \quad |p_e| \le \widetilde{m}Y \\ \dfrac{\eta_s}{\phi_0}\dfrac{|p_e|}{Y}\exp(1-|p_e|/(Y\widetilde{m})) & \text{if} \quad |p_e| > \widetilde{m}Y \end{cases}. \tag{30}$$

Use of this expression in equation (21) yields phase trajectories of the form:

$$\exp\left(\left|\frac{p_e}{Y\widetilde{m}}\right| - 1\right) - \frac{1}{2} = \omega\widetilde{m}\left(\frac{p^*}{Y}\right)^2 h(\varphi) \quad \text{if} \quad |p_e| > \widetilde{m}Y. \tag{31}$$

For $|p_e| \le \widetilde{m}Y$, phase trajectories are given by equation (27). Figure 6 shows the porosity wave in pressure-insensitive viscoplastic porous matrix (solid line). For comparison, a pure viscous solution is plotted as a dotted line. Plasticity preserves the solitary wave solution but alters its properties. In the presence of pressure-insensitive yield, the amplitude of the wave is preserved but the wavelength is reduced. This is because plasticity reduces the effective viscosity, which reduces the viscosity contrasts between solid and fluid. Note that a reduction in ω equivalent to a reduction in viscosity contrast in pure viscous waves also reduces the wavelength of the solitary wave (Figure 5). Plasticity reduces the amplitude of the pressure anomaly. The impact of plasticity on the porosity wave strongly depends on the magnitude of the yield stress. The decrease in the yield stress (=more pronounced plastic flow) causes a stronger reduction in the wavelength and in the amplitude of the pressure anomaly. High values of the yield stress would only slightly alter the viscous wave (Figure 6).

3.4. Viscoplastic Matrix With Dilatant Brittle Failure

Effective viscosity for viscoplastic rocks with dilatant brittle failure takes the form:

$$\eta_\varphi = \begin{cases} \widetilde{m}\eta_s/\phi_0 & \text{if} \quad \left|\dfrac{p_e}{Y^*}\right| \le \dfrac{\widetilde{m}}{2\kappa} \\ \dfrac{2\eta_s\kappa}{\varphi_0}\dfrac{p_e}{Y^*}\left(1 + \dfrac{\left(\widetilde{P}^\gamma - 1\right)(\kappa + m)}{\gamma m(1-\kappa)}\right) & \text{if} \quad \left|\dfrac{p_e}{Y^*}\right| > \dfrac{\widetilde{m}}{2\kappa} \end{cases}. \tag{32}$$

Table 3. Shorthand Notations

$Y^* = 2\xi \cos\phi Y/(1+\xi \sin\phi)$
$\kappa = (1-\xi \sin\phi)/(1+\xi \sin\phi)$
$\varsigma = (1-\xi \sin\psi)/(1+\xi \sin\psi)$
$\gamma = 1-\kappa/(\kappa-1)\cdot(1/\varsigma+1/m)$
$\chi = (\kappa+m)/(m(1-\kappa))$
$\tilde{m} = 2m/(m+1)$

Parameters Y^* and κ reflect the failure properties of the rock matrix as well as the sign of loading (compaction or decompaction; see also Table 3 for notations). This leads to different yield limits and effective viscosities for compaction and decompaction. Viscous compaction takes place for $p_e < \sqrt{3}Y$ or $p_e < 4\sqrt{3}Y/3$ depending on pore geometry, while viscous decompaction proceeds as long as $p_e > -Y/\sqrt{3}$ or $p_e > -4\sqrt{3}Y/9$. Before the yield stress is reached, the phase trajectories are defined by equation (27), while in the plastic regime:

$$-\left(\frac{Y}{p^*}\right)^2 \frac{3\sqrt{3}p_e + Y}{\sqrt{3}p_e + 3Y} = 6\omega h(\varphi) \quad if \quad p_e < -\frac{Y}{\sqrt{3}} \quad \text{(decompaction)}$$

$$\frac{(p_e + \sqrt{3}Y)^3}{6\sqrt{3}Y(p^*)^2} - \left(\frac{Y}{p^*}\right)^2 = 2\omega h(\varphi) \quad if \quad p_e > \sqrt{3}Y \quad \text{(compaction)}$$

for cylindrical pores and

$$\left(\frac{Y}{p^*}\right)^2 \left(\frac{2}{3}\left(\frac{5}{3}\right)^{5/4}\left(3+\sqrt{3}\frac{p_e}{Y}\right)^{-1/4} - 1\right) = \frac{\omega}{2}h(\varphi) \quad if \quad p_e < -\frac{4\sqrt{3}}{9}Y \quad \text{(decompaction)}$$

$$\left(\frac{Y}{p^*}\right)^2 \left(\frac{2}{3}\frac{1}{7^{7/4}}\left(3+\sqrt{3}\frac{p_e}{Y}\right)^{11/4} - 1\right) = \frac{11}{6}\omega h(\varphi) \quad if \quad p_e > \frac{4\sqrt{3}}{3}Y \quad \text{(compaction)}$$

for spherical pores. For simplicity, we assumed here that the angle of internal friction is $\varphi = \pi/6$ and the dilatancy angle is $\psi = 0$. A numerical solution of compaction equation (21) for viscoplastic matrix with dilatant brittle failure shows that asymmetry in the effective viscosity (equation (32)) leads to a strong asymmetry of the wave —this significantly reduces the overpressure required for wave propagation (Figure 7). The amplitude of the wave in the (φ, z) plane is not affected by the presence of brittle failure in a small-porosity limit (Figure 7, left).

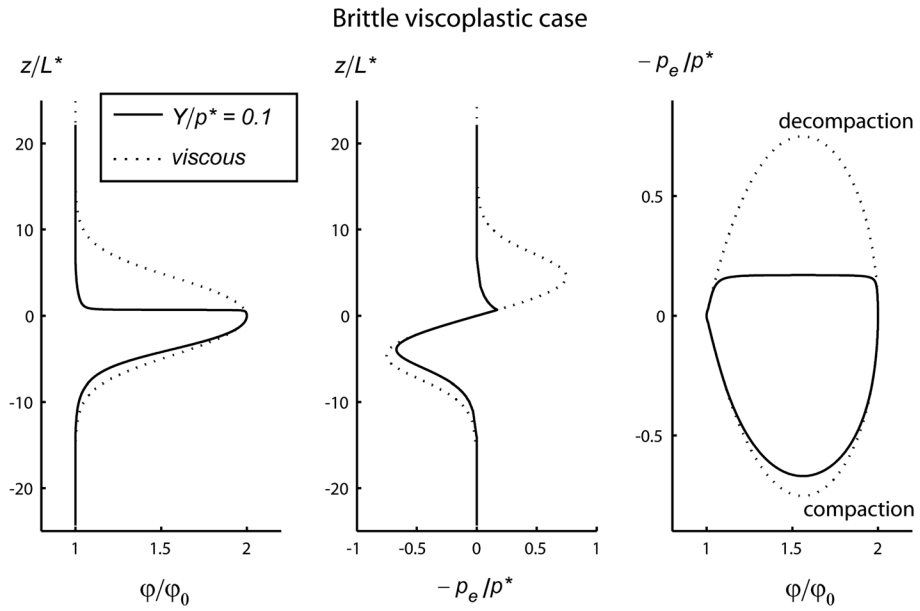

Figure 7. Analytical stationary solution for porosity and effective pressure distribution within solitary wave in a viscoplastic matrix with dilatant brittle failure ($\omega = 5$, $n = 3$). The dotted lines correspond to purely viscous solution obtained for the same values of parameters.

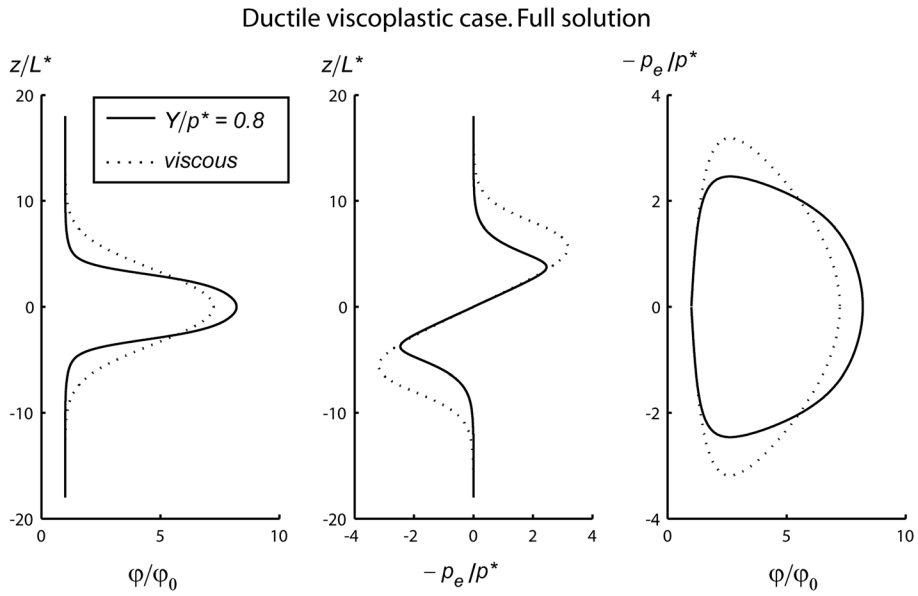

Figure 8. Viscoplastic solution to full compaction equations in a matrix with pressure-insensitive yielding ($\omega = 10$, $n = 3$, $\phi_0 = 0.01$): porosity profile with depth, fluid pressure anomaly profile with depth, and corresponding phase diagram. The dotted line corresponds to the purely viscous solution to full compaction equations obtained for the same values of sedimentation parameter, permeability exponent, and background porosity.

4. Steady State Compaction: Full Solutions

In some cases, the full compaction equations can be integrated exactly. If we accept the Carman-Kozeny porosity-permeability relationship in the form:

$$k = k_0 \left(\frac{\varphi}{\varphi_0}\right)^3 \left(\frac{1-\varphi_0}{1-\varphi}\right)^2, \tag{33}$$

then the solution of the purely viscous compaction equations will take the form of equation (27) where the hydraulic potential and characteristic scales are modified versus the small-porosity, such that

$$h(\varphi) = \omega(\varphi-\varphi_0)^2 \frac{\varphi+2\varphi_0}{6\varphi^3} - (1-\varphi_0)\ln\frac{\varphi}{\varphi_0} - \frac{\varphi-\varphi_0}{3\varphi}\left((3\varphi_0-2)\frac{\varphi+\varphi_0}{2\varphi} - \frac{{\varphi_0}^2}{\varphi^2}\right)$$

$$L^* = \sqrt{\frac{k_0\eta_s}{\varphi_0\eta_f}(1-\varphi_0)} \tag{34}$$

$$p^* = \Delta\rho g L^*. \tag{35}$$

However, no analytical solutions are available in a viscoplastic case, and only numerical solutions to full compaction equations are possible. At nonnegligible porosities, plastic failure has a much stronger impact on the porosity wave than in the case of small porosities (Figure 8). This affects not only the wavelength and the magnitude of the pressure anomaly but also increases the amplitude of the wave. Comparison of the full and approximate solutions from previous sections shows that the small-porosity approximation gives acceptable predictions for $\varphi \leq 1\,\%$.

At low-yield stresses and high-sedimentation parameter ω values, the fluid overpressure generated by the porosity wave can eventually meet the criterion for the full plastic pore collapse. Such a system is given as the upper pressure limit in Table 2. As this occurs, the viscoplastic porosity equation (5) has to be substituted by one of the equations of full plastic pore collapse listed in Table 2. Full pore collapse precludes further pressure buildup and creates a propagating upward shock wave (Figure 9). The amplitude of the shock is fully controlled by the hydraulic potential. Unlike viscous and viscoplastic porosity waves, plastic shock waves do not detach from the source region. That is, it does not restore the initial background values of pressure and porosity below the wave.

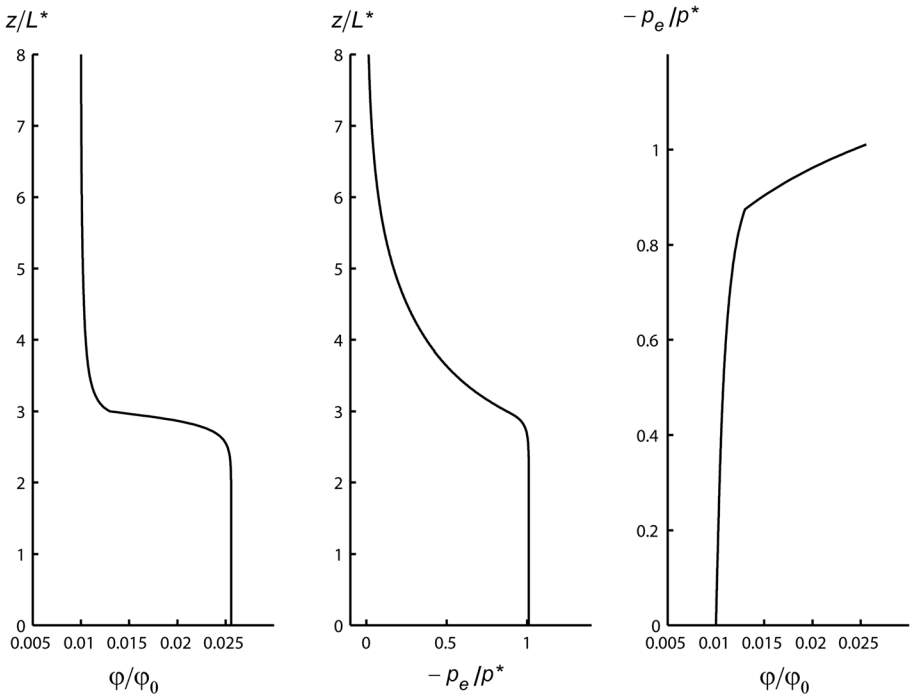

Figure 9. Shock wave solution to full compaction equations in a purely plastic matrix with pressure-insensitive yielding ($\omega = 10$, $n = 3$, $\phi_0 = 0.01$, $Y/p^* = 0.2$): porosity and fluid pressure anomaly profiles with depth and corresponding phase diagram.

5. Speed, Amplitude, and Excess Volume of Porosity Wave

5.1. Small Porosities

We next examine the relationship between the fluid volume carried by the porosity wave including its speed and amplitude. As we noticed in the previous section, developing plastic flow in a low-porosity limit does not change the amplitude of porosity waves. The viscoplastic trajectory in the phase plane (φ, p_e) starts from a trajectory of viscous solution and returns to exactly the same viscous trajectory as pressure drops below the yield point (Figures 6 and 7, right). Thus, to find the relationship between the maximum amplitude, A, of the viscoplastic porosity wave and its nondimensional speed, ω, we put $p_e = 0$ at $\varphi/\varphi_0 = A$ in equation (27). This also defines purely viscous waves. These results in the following dispersion relation are for one-dimensional waves in a small-porosity limit:

$$\omega = 1 + 2A. \tag{36}$$

Thus, plastic flow does not affect wave speed unless the background porosity is high.

It is known that porosity waves arise in response to an obstruction to fluid flow when a critical amount of fluid gets trapped in the pore space. The fluid volume carried by the wave can be defined in terms of the excess volume, which is a volume of fluid-filled porosity above the background level integrated over the source region:

$$V_{\text{exc}} = \int_{-\infty}^{+\infty} (\varphi - \varphi_0) dz. \tag{37}$$

Excluding depth from the last equation via equation (20), one can rewrite excess volume in terms of the porosity integral, namely,

$$V_{\text{exc}} = \int_{\varphi_0}^{\varphi_{\max}} (\varphi - \varphi_0) \frac{dz}{d\varphi} d\varphi = q_s \int_{\varphi_0}^{\varphi_{\max}} (\varphi - \varphi_0) \frac{\eta_\varphi(\varphi)}{p_e(\varphi)} d\varphi.$$

Excess volume contained in the source region affects the wave amplitude, which in turn determines the wave speed according to equation (36). Therefore, a direct relationship between wave speed and amount of fluid

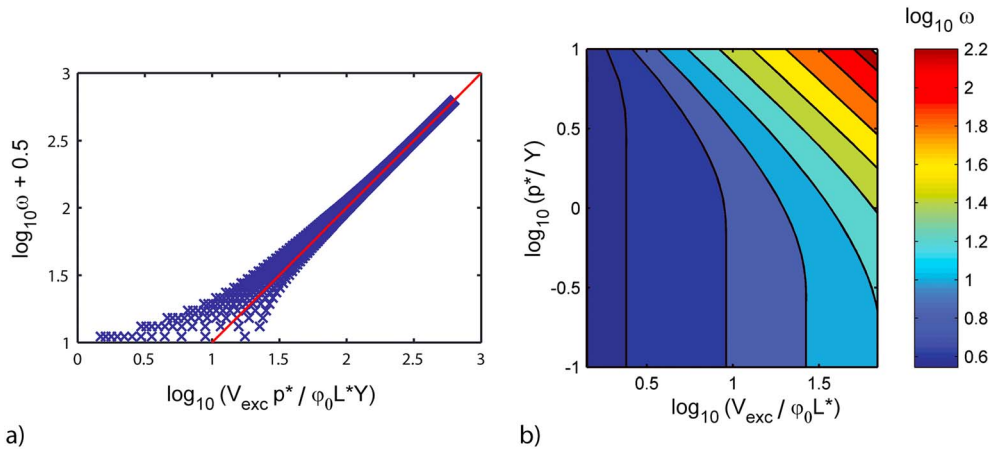

Figure 10. Dimensionless wave speed as a function of excess volume available in the source region and the extent of pressure-insensitive plastic flow defined by the ratio of the characteristic pressure p^* to the matrix yield strength Y (small-porosity approximation). (a) Collapse of data (blue crosses) for wave speed ω at different values of V_{exc} and $p^*/Y > 1$ on a single master curve (red line). The results are presented for two different deformation modes, namely, viscous corresponding to low values of ω and viscoplastic at large ω. Wave speed has a different dependence on pressure and porosity for both regimes, which explains the scatter of data at low values of ω. (b) Dependence of dimensionless wave speed ω on the dimensionless yield stress and excess volume. At high-yield strength and low V_{exc} solitary wave will be purely viscous. Notice that at low values of V_{exc} and p^*/Y (lower left corner of the diagram), the level set is vertical, which indicates that velocity is independent of p^*/Y and corresponds to purely viscous waves.

available for generation of porosity waves can be obtained (Figures 10 and 11). The excess volume also reduces the presence of yielding because in a small-porosity case, the plastic flow reduces the wavelength of the wave but does not alter its amplitude. The extent of plastic flow caused by the wave depends on the wave amplitude and strength of the matrix material. Decreasing yield stresses increases the ability of the solid matrix to yield. In a matrix with lower-yield stress, the plastic flow will be more pronounced and waves would be more focused. Accordingly, the excess volume carried by such a wave would be smaller versus a nonyielding matrix. Plastic yielding of the solid matrix reduces the excess volume necessary to generate a porosity wave with a certain wave speed. Waves generated from a larger source travel faster. Decreasing yield strength (cohesion) aids the onset of plastic yielding during wave propagation and

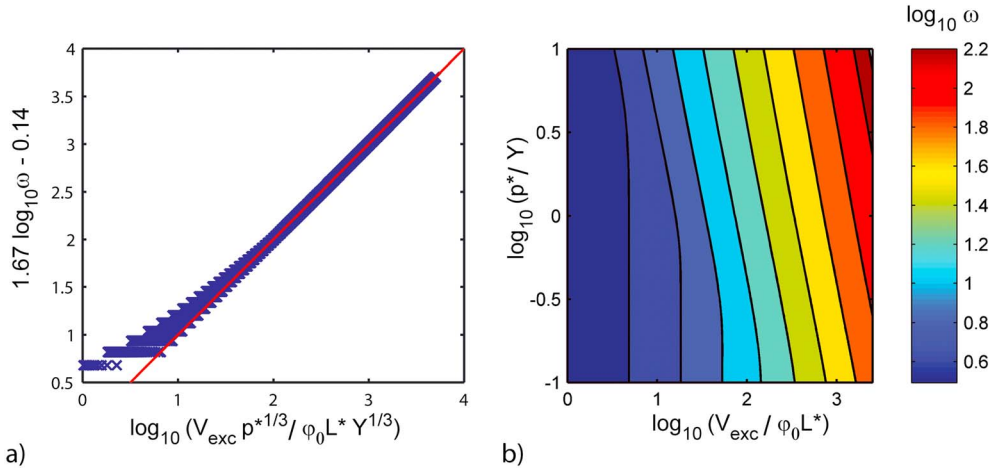

Figure 11. Dimensionless wave speed as a function of excess volume available in the source region and the extent of dilatant brittle failure (small-porosity approximation). (a) Collapse of data (blue crosses) for wave speed ω at different values of V_{exc} and $p^*/Y > 10$ on a single master curve (red line). The scatter of data at low values of ω is explained by the absence of plastic flow. (b) Dependence of dimensionless wave speed ω on the ratio p^*/Y and excess volume. Notice that at low values of V_{exc} and p^*/Y (lower left corner of the diagram), the level set is vertical, which indicates that velocity is independent of p^*/Y and corresponds to purely viscous waves.

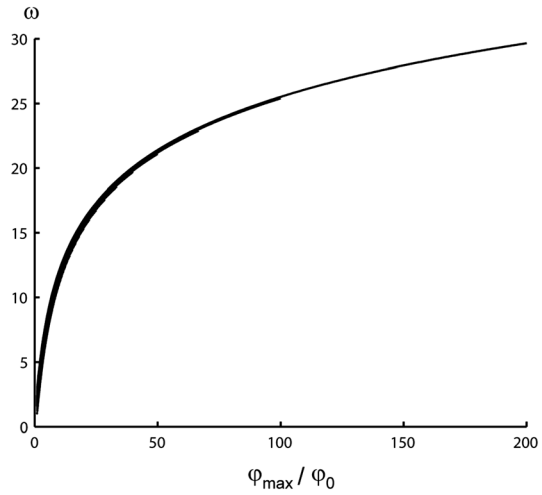

Figure 12. Phase speed of porosity wave as a function of its amplitude $A = \phi_{max}/\phi_0$ for different values of background porosity calculated according to the purely viscous solution to full compaction equations.

decreases the excess volume necessary to generate a wave propagating with a given speed ω. Viscoplastic waves travel faster than purely viscous waves generated from the source with the same excess volume (Figures 10b and 11b). In turn, their amplitudes are higher. For $p^*/Y > 1$, the speed of the wave in a pressure-insensitive viscoplastic matrix can be approximated as (Figure 10a):

$$\omega = \frac{V_{exc}}{\sqrt{10}\varphi_0 L^*}\frac{p^*}{Y}.$$

In a viscoplastic matrix with dilatant brittle failure, the speed of the wave for $p^*/Y > 10$ can be approximated as (Figure 11a):

$$\omega^{1.67} = 10^{0.14}\frac{V_{exc}}{\varphi_0 L^*}\left(\frac{p^*}{Y}\right)^{1/3}.$$

5.2. Full Solution

The dispersion relation (equation (36)) is linear at a small-porosity limit. However, at higher values of background porosity, the dependence of bulk viscosity on porosity strongly influences the dispersion relation [*Barcilon and Richter*, 1986; *Connolly and Podladchikov*, 2007]. This results in the following nonlinear dependence of the purely viscous wave speed on its amplitude and background porosity:

$$\omega = \frac{6A^3(1-\varphi_0)}{(A+2)(A-1)^2}\ln A - \frac{A(A+1)(2-3\varphi_0)+2}{(A+2)(A-1)}. \quad (38)$$

Wave amplitude, A, is the main factor controlling the speed of the wave, while variations in φ_0 lead only to slight deviations from the main trend (notice the thickening of the master curve at small values of the amplitude in Figure 12). At large A values, equation (38) simplifies leading to the following dispersion relationship:

$$\omega = 6(1-\varphi_0)\ln A - 2.$$

For viscoplastic rocks, the bulk viscosity is a nonlinear function of porosity. Therefore, plasticity affects the wave speed in the case of large and moderate background porosities $\varphi > 1\,\%$ (Figure 13). As in a small-porosity limit, the excess volume necessary to generate a porosity wave in a viscoplastic matrix is smaller than the excess volume needed for the purely viscous case. At low values of p^*/Y and V_{exc}, the amplitude

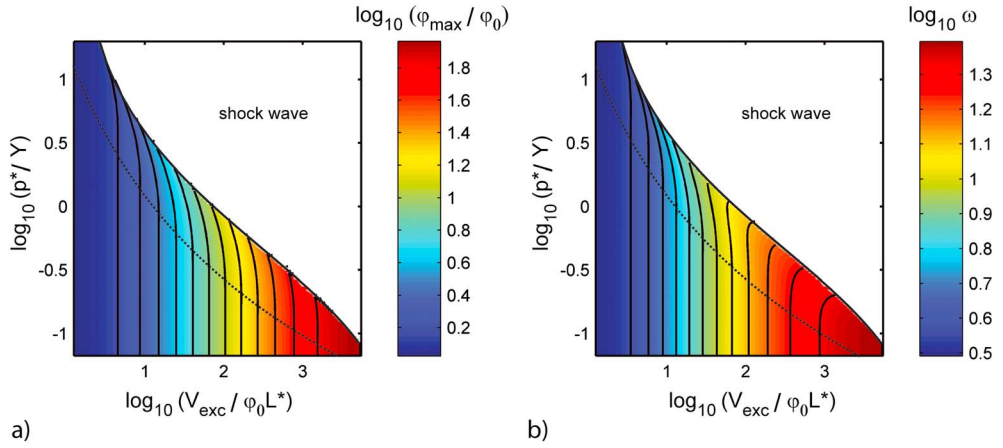

Figure 13. Amplitude and velocity of porosity wave in a pressure-insensitive viscoplastic matrix (full solution obtained for $\phi_0 = 0.01$). (a) Dependence of the dimensionless wave amplitude on the ratio p^*/Y and excess volume. (b) Dependence of the dimensionless wave speed on the ratio p^*/Y and excess volume.

and speed are independent of p^*/Y, and the wave is purely viscous (note the vertical level sets of amplitude and speed in Figure 13). Waves generated from the larger source would travel faster. Plastic yielding increases the amplitude of the wave versus the purely viscous wave generated from the same source.

Fast-propagating porosity waves can even eventually develop full pore collapse due to significant increases in fluid pressure. This is especially true if the yield strength of the matrix is low or the excess volume is high (note the white area in Figure 13). As this occurs, porosity wave degenerates into a shock wave. As a result, in a matrix with nondilute levels of background porosity, the viscoplastic porosity waves can be generated only in a limited range of p^*/Y and $V_{exc}/\varphi_0 L^*$. This corresponds to a narrow area adjacent to the shock wave zone where the level set diverges from the vertical direction.

6. Conclusions

We formulated a mathematical model of segregation and migration of fluids in a viscoplastic compacting porous matrix consistent with thermodynamics and microscale physics. We studied porosity waves propagating through the matrix of low and moderate background porosity. The model predicted that the solitary porosity waves can propagate through a viscoplastic porous matrix. In general, viscoplastic waves resemble the purely viscous waves studied in the literature. However, the presence of plastic yielding alters their properties and brings some new phenomena. Plastic yielding reduces the wavelength and increases the amplitude of the wave. The pressure anomaly within the viscoplastic wave is significantly reduced versus the purely viscous case. Thus, only moderate overpressures are generated by the wave. Viscoplastic waves generated from the source with the same excess volume travel faster than purely viscous ones. Porosity waves generated in rocks exhibiting decompaction weakening are strongly asymmetric. Previously, this asymmetry was shown to cause strong flow channeling [*Connolly and Podladchikov*, 2007]. Shock waves are observed in a purely plastic regime of matrix deformation. The velocity and the amplitude of a porosity wave are given as functions of the ability of a solid matrix to yield and the volume of the fluid-filled porosity in excess of a background value. We identified parameter values at which purely viscous, viscoplastic, or purely plastic waves can generate. Purely viscous waves arise from small sources in the matrix with high-yield strength. Weak rocks of moderate background porosity accommodate only purely plastic shocks due to their inability to sustain high hydraulic pulses. Viscoplastic waves of finite amplitude are generated only at limited values of parameters. However, viscous, viscoplastic, and plastic waves can transform into each other while propagating. The proposed formulation is applicable to melt migration in the Earth's deep interiors, fluid migration in sedimentary basins, as well as CO_2 upward migration at injection sites.

Appendix A: The Oscillating Ball Analogy

A1. Phase Portrait, First Integral, and Direction Field

Integration of equation (24) for an oscillating ball in a closed form is not always possible depending on the complexity of the surface geometry h. However, even without integration one can learn about the qualitative behavior of the solution from its phase portrait and a direction field. For any t, the position of the ball on the surface h and its velocity can be represented as a point on a phase plane (x, v). When the ball starts to move its position x and velocity v change, and the point (x, v) moves along a phase trajectory (Figures 4 and A1).

All phase trajectories of equation (24) correspond to different initial conditions and can be obtained as solutions to equation:

$$\frac{dv}{dx} = -\frac{\partial h}{\partial x}\frac{g}{v} \tag{A1}$$

that follows from equation (24) after excluding time. Separation of variables in equation (A1) leads to

$$v\,dv + g\frac{\partial h}{\partial x}dx = 0.$$

The final equation can be easily integrated, such that

$$E = v^2/2 + gh, \tag{A2}$$

where E is the total energy of the ball, which is conserved along trajectories. The energy of the ball E is determined by its initial position x_{ini} on the surface h and its initial velocity v_{ini} (Figure 3). The contour plots

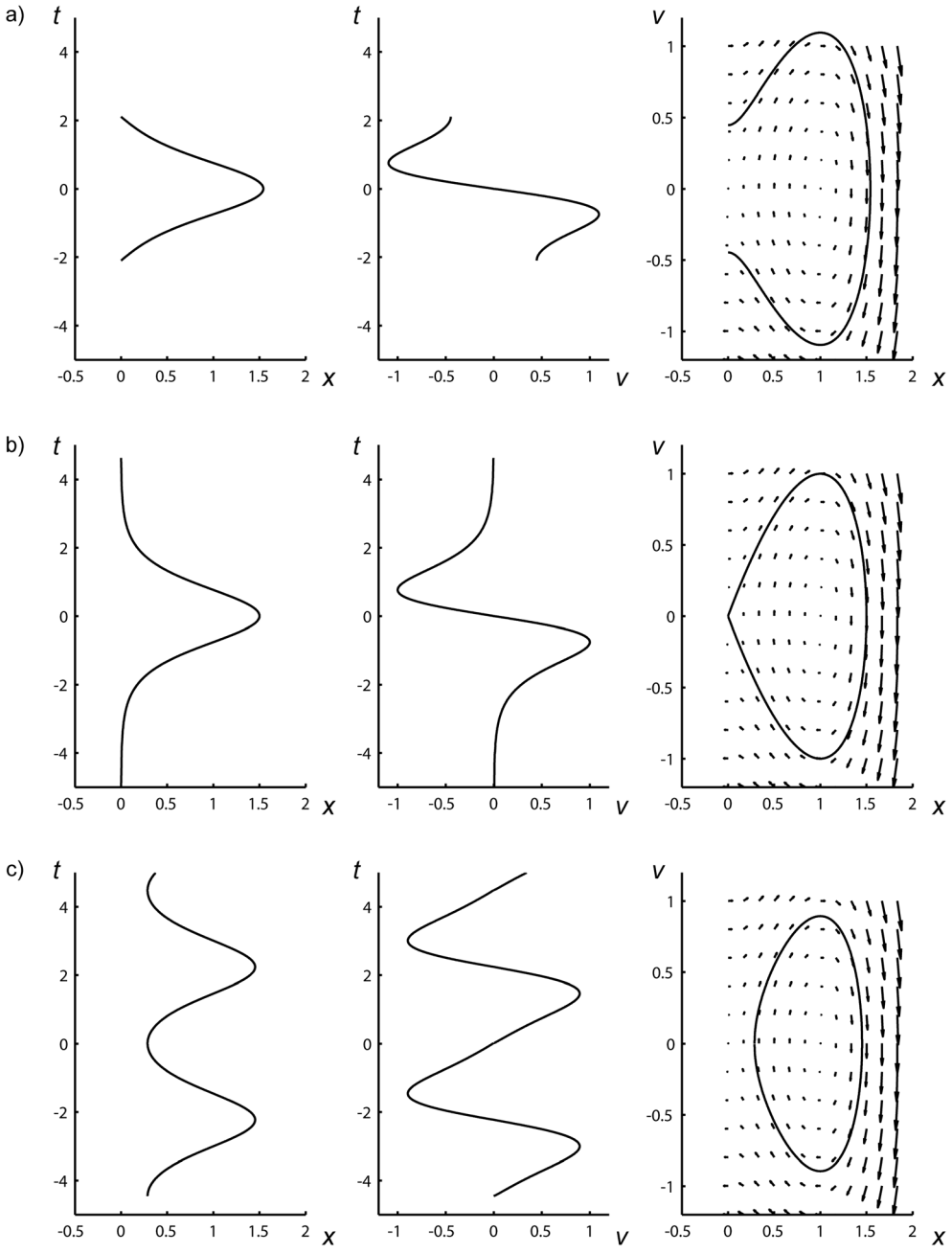

Figure A1. Solutions and phase portraits for equations governing the oscillations of a ball on a curved surface corresponding to three different total energy levels. (a) The solution with open phase trajectory (the uppermost plot) corresponds to the ball with total energy E_2 that is higher than the critical value E_c (Figure 3). (b) Solution with self-intersecting phase trajectory. (c) A periodic solution with closed phase trajectory is obtained for a ball with initial position x_1, and zero velocity providing the ball has total energy E_1 lower than critical value E_c.

of energy in the plane (x, v) define implicit dependence $v(x)$ and give all possible phase trajectories for equation (24).

The evolution of x and v with time can be shown by imposing the direction field $(dx/dt, dv/dt)$ on top of a phase trajectory. The plot of possible phase trajectories and corresponding direction fields constitutes a phase portrait (Figure A1). Its structure shows the quantitative features of ball behavior on the curved surface.

Equations (24) and (A1) have a special solution that is not described by the energy integral (equation (A2)). It corresponds to equilibrium points where the ball is motionless, such that

$$\frac{dx}{dt} = 0 \quad \text{and} \quad \frac{dv}{dt} = 0.$$

Equilibrium points separate regions where solutions to equations (24) and (A1) have different quantitative behavior and therefore are very important for the structure of the phase portrait.

A2. Example: Cubic Shape Function

As a simple example, let us consider $h = x^2(x - 3/2x_0)$ with $x_0 > 0$ (Figure 3a). The equation $\partial h/\partial x = 3x(x - x_0) = 0$ has two roots, which means that the oscillating ball equation (24) have two equilibrium points. The first point $x = x_0\ \left(h = -x_0^3/2\right)$ corresponds to a minimum on the curve h. This is a point of stable equilibrium. If external forces cause a slight deviation of the ball from the position of stable equilibrium it begins to oscillate around this point trying to return to its initial position. Another equilibrium point, $x = 0\ (h = 0)$, is a point of unstable equilibrium and corresponds to the maximum on the curve h. Being placed in this position, the ball remains there in the absence of external interference, but if slightly disturbed the ball slides away. Contour plots of the total energy, E, and the corresponding direction fields are very different for these situations and correspond to different special solutions (Figure A1). A self-intersecting homoclinic orbit separates the phase plane (x, v) into two different domains. There are closed curves inside the homoclinic orbit trajectories, and the outside trajectories are open. Each type of phase trajectory corresponds to a certain mode of ball motion. All phase trajectories are symmetrical with respect to the line $v = 0$. In the upper half of the phase plane the velocity is positive and corresponds to the motion of the ball to the right. The lower half of the phase plane corresponds to the leftward motion.

A2.1. Closed Trajectories: Periodic Motion

Let us consider a ball initially placed in position $x_1 < x_c$. Its initial state is characterized by a point $(x_1, v_1 = 0)$ lying inside the homoclinic orbit on a closed trajectory (Figure 3a). The ball oscillates between the initial position x_1 and a position of equal height at which its kinetic energy vanishes (Figure 3a). During the motion, the ball maintains its total energy $E_1 < E_c$. The behavior of the ball is periodic, and a solution to equation (24) is also periodic (Figure A1a).

A2.2. Open Trajectories: Nonwave Solutions

Now consider the ball initially placed at $x_2 > x_c$. Its initial state is given by the point $(x_2, v_2 = 0)$ lying on an open trajectory outside the homoclinic orbit. On the surface h, the ball is placed above the critical level $h = 0$ corresponding to $x_2 > x_c$. During the motion, the ball maintains the total energy $E_2 > E_c$. Once it starts sliding from its initial position, such a ball would have enough energy to overcome the barrier at $x = 0$ and to go infinitely far away from the initial position. Correspondingly, x and v are unlimited functions of time (Figure A1b).

A2.3. Self-Intersecting Trajectory: Solitary Wave Solution

Imagine now the ball with initial state on the homoclinic orbit $(x_c = 3/2x_0, v_c = 0)$. Such a ball possesses the critical energy level E_c. Set in motion, the ball has enough energy to climb the hill at $x = 0$. However, it takes an infinitely long time for it to do so. The behavior of x and v with time is shown on Figure A1c. The shape of the x-t curve resembles a solitary wave.

Whether or not periodic or solitary wave solutions are possible for the oscillating ball depends on the shape of the surface. If it is convex, then only periodic solutions are possible. If it is concave then all solutions are nonbounded, nonperiodic functions of time. Solitary wave solutions are possible only if the surface h has a potential well and inflection points defined as roots of the equation $\partial^2 h/\partial x^2 = 0$ at which $\partial^2 h/\partial x^2$ changes sign. The shape of the function h determines both the amplitude and the stability of oscillations, whereas the gravitational constant controls the velocity of the ball and therefore the period of oscillation.

Acknowledgments
We are grateful to Harro Schmeling and Einat Aharonov for their helpful discussions and comments. This work is purely theoretical and makes no use of any specific data other than standard mathematical models described above. All the results of the paper can be reproduced following derivations specified in the text of the paper. This work was supported in part by a grant (193825/S60) from the Norwegian Research Council and IFE's strategic funds.

References

Aharonov, E., M. Spiegelman, and P. Kelemen (1997), Three-dimensional flow and reaction in porous media: Implications for the Earth's mantle and sedimentary basins, *J. Geophys. Res.*, *102*(B7), 14,821–14,833, doi:10.1029/97JB00996.

Appold, M. S., and J. A. Nunn (2002), Numerical models of petroleum migration via buoyancy-driven porosity waves in viscously deformable sediments, *Geofluids*, *2*(3), 233–247.

Barcilon, V., and F. M. Richter (1986), Nonlinear waves in compacting media, *J. Fluid Mech.*, *164*, 429–448.
Barcilon, V., and O. M. Lovera (1989), Solitary waves in magma dynamics, *J. Fluid Mech.*, *204*, 121–133.
Bercovici, D., Y. Ricard, and G. Schubert (2001), A two-phase model for compaction and damage 1. General theory, *J. Geophys. Res.*, *106*(B5), 8887–8906, doi:10.1029/2000JB900430.
Biot, M. A. (1941), General theory of three-dimensional consolidation, *J. Appl. Phys.*, *12*(2), 155–164.
Cai, Z. Y., and D. Bercovici (2013), Two-phase damage models of magma-fracturing, *Earth Planet. Sci. Lett.*, *368*, 1–8.
Connolly, J. A. D. (1997), Devolatilization-generated fluid pressure and deformation-propagated fluid flow during regional metamorphism, *J. Geophys. Res.*, *102*(B8), 18,149–18,173, doi:10.1029/97JB00731.
Connolly, J. A. D., and Y. Y. Podladchikov (1998), Compaction-driven fluid flow in viscoelastic rock, *Geodin. Acta*, *11*(2–3), 55–84.
Connolly, J. A. D., and Y. Y. Podladchikov (2000), Temperature-dependent viscoelastic compaction and compartmentalization in sedimentary basins, *Tectonophysics*, *324*(3), 137–168.
Connolly, J. A. D., and Y. Y. Podladchikov (2007), Decompaction weakening and channeling instability in ductile porous media: Implications for asthenospheric melt segregation, *J. Geophys. Res.*, *112*, B10205, doi:10.1029/2005JB004213.
Connolly, J. A. D., and Y. Y. Podladchikov (2013), A hydromechanical model for lower crustal fluid flow, in *Metasomatism and the Chemical Transformation of Rock: The Role of Fluids in Terrestrial and Extraterrestrial Processes*, edited by D. E. Harlov and H. Austrheim, pp. 599–658, Springer, Berlin, Heidelberg.
Connolly, J. A. D., and Y. Y. Podladchikov (2015), An analytical solution for solitary porosity waves: Dynamic permeability and fluidization of nonlinear viscous and viscoplastic rock, *Geofluids*, *15*(1–2), 269–292.
Gassmann, F. (1951), Über die elastizität poröser medien, *Vierteljahrschr. Naturforsch. Ges. Zürich*, *96*, 1–23.
Kumagai, I., and K. Kurita (2015), Buoyancy-driven flows in deformable porous media, paper presented at EGU General Assembly, Vienna.
Loseth, H., L. Wensaas, B. Arntsen, N. M. Hanken, C. Basire, and K. Graue (2011), 1000 m long gas blow-out pipes, *Mar. Petrol. Geol.*, *28*(5), 1047–1060.
Mckenzie, D. (1984), The generation and compaction of partially molten rock, *J. Petrol.*, *25*(3), 713–765.
McKenzie, D. (2000), Constraints on melt generation and transport from U-series activity ratios, *Chem. Geol.*, *162*(2), 81–94.
Nguyen, S. H., A. I. Chemenda, and J. Ambre (2011), Influence of the loading conditions on the mechanical response of granular materials as constrained from experimental tests on synthetic rock analogue material, *Int. J. Rock Mech. Min. Sci.*, *48*(1), 103–115.
Olson, P., and U. Christensen (1986), Solitary wave-propagation in a fluid conduit within a viscous matrix, *J. Geophys. Res.*, *91*(B6), 6367–6374, doi:10.1029/JB091iB06p06367.
Plaza-Faverola, A., S. Bunz, and J. Mienert (2011), Repeated fluid expulsion through sub-seabed chimneys offshore Norway in response to glacial cycles, *Earth Planet. Sci. Lett.*, *305*(3–4), 297–308.
Raess, L., V. M. Yarushina, N. S. C. Simon, and Y. Y. Podladchikov (2014), Chimneys, channels, pathway flow or water conducting features—An explanation from numerical modelling and implications for CO_2 storage, *Energy Procedia*.
Rice, J. R. (1992), Fault stress states, pore pressure distributions and the weakness of the San Andreas fault, in *Fault Mechanics and Transport Properties of Rocks*, edited by B. Evans and T.-F. Wong, pp. 475–503, Academic Press, New York.
Richter, F. M., and D. Mckenzie (1984), Dynamical models for melt segregation from a deformable matrix, *J. Geol.*, *92*(6), 729–740.
Sayers, C. M., and P. M. T. M. Schutjens (2007), An introduction to reservoir geomechanics, *Leading Edge*, *26*, 597–601.
Schmeling, H. (2000), Partial melting and melt segregation in a convecting mantle, in *Physics and Chemistry of Partially Molten Rocks*, edited by N. Bagdassarov, D. Laporte, and A. B. Thompson, pp. 141–178, Kluwer Acad., Dordecht, Netherlands.
Scott, D. R., and D. J. Stevenson (1984), Magma solitons, *Geophys. Res. Lett.*, *11*(11), 1161–1164, doi:10.1029/GL011i011p01161.
Scott, D. R., and D. J. Stevenson (1986), Magma ascent by porous flow, *J. Geophys. Res.*, *91*(B9), 9283–9296, doi:10.1029/JB091iB09p09283.
Scott, D. R., D. J. Stevenson, and J. A. Whitehead (1986), Observations of solitary waves in a viscously deformable pipe, *Nature*, *319*(6056), 759–761.
Simpson, G., and M. I. Weinstein (2008), Asymptotic stability of ascending solitary magma waves, *Siam J. Math. Anal.*, *40*(4), 1337–1391.
Slater, L., D. McKenzie, K. Gronvold, and N. Shimizu (2001), Melt generation and movement beneath Theistareykir, NE Iceland, *J. Petrol.*, *42*(2), 321–354.
Spiegelman, M. (1993), Physics of melt extraction—Theory, implications and applications, *Philos. Trans. R. Soc. London, Ser. A: Math. Phys. Eng. Sci.*, *342*(1663), 23–41.
Sramek, O., Y. Ricard, and D. Bercovici (2007), Simultaneous melting and compaction in deformable two-phase media, *Geophys J Int.*, *168*(3), 964–982.
Sumita, I., S. Yoshida, M. Kumazawa, and Y. Hamano (1996), A model for sedimentary compaction of a viscous medium and its application to inner-core growth, *Geophys. J. Int.*, *124*(2), 502–524.
Tantserev, E., C. Y. Galerne, and Y. Y. Podladchikov (2009), Multiphase flow in multi-component porous visco-elastic media, paper presented at Poro-Mechanics IV.
Tian, M., and J. J. Ague (2014), The impact of porosity waves on crustal reaction progress and CO_2 mass transfer, *Earth Planet. Sci. Lett.*, *390*, 80–92.
Vasilyev, O. V., Y. Y. Podladchikov, and D. A. Yuen (1998), Modeling of compaction driven flow in poro-viscoelastic medium using adaptive wavelet collocation method, *Geophys. Res. Lett.*, *25*(17), 3239–3242, doi:10.1029/98GL52358.
von Terzaghi, K. (1923), Die berechnung der durchlassigkeit des tones aus dem verlauf der hydromechanischen spannungserscheinungen, *Sitzungsber. Akad. Wissensch. Mach.-Naturwiss. Klasse*, *132*, 125–138.
Wickham, S. M. (1987), The segregation and emplacement of granitic magmas, *J. Geol. Soc. London*, *144*, 281–297.
Wurbs, R. A. (1993), Reservoir-system simulation and optimization models, *J. Water Res. Pl. ASCE*, *119*(4), 455–472.
Yarushina, V. M., and Y. Y. Podladchikov (2015), (De)compaction of porous viscoelastoplastic media: Model formulation, *J. Geophys. Res. Solid Earth*, *120*, doi:10.1002/2014JB011258.